Environ Earth Sci (2016) 75:73
DOI 10.1007/s12665-015-4938-x

ORIGINAL ARTICLE

Diurnal pattern of liquid water and water vapor movement affected by rainfall in a desert soil with a high water table

Jinting Huang[1,2] · **Rongzhe Hou**[3] · **Hongbin Yang**[2]

Received: 19 March 2015 / Accepted: 20 August 2015 / Published online: 21 December 2015

Abstract Because arid and semi-arid regions have relatively low soil moisture, water vapor movement often occurs predominantly in the unsaturated zone, affecting the partitioning of energy among various land surface fluxes. To understand the hydrological processes of the unsaturated zone in desert areas, it is important to characterize the diurnal and spatial variations in soil water and vapor movement, which control recharge and discharge via the unsaturated zone. However, few studies have examined the pattern of soil water and vapor movement affected by rainfall in desert areas. To understand this process, field observations of desert soil physical parameters and micrometeorological variables were taken. These data were used to verify and calibrate the performance of an unsaturated–saturated zone soil water balance model, Hydrus-1D. Next, the diurnal pattern of the soil water and vapor was simulated under different climatic conditions, i.e., before, during and after rainfall. Two stages of thermal liquid and vapor movement were identified before rainfall. The thermal liquid flux fluctuates quickly and drastically, while the thermal vapor changes more moderately during and after rainfall. The changes in isothermal liquid and vapor flux differ from those of thermal liquid and vapor flux because of the change in the pressure head gradient under various wetness conditions. These findings offer insight into how water vapor affects soil water movement in the semiarid desert. They also improve our understanding of the liquid water and water vapor movement processes following rainfall.

Keywords Vadose zone · Liquid water and water vapor flow · Heat transport · Rainfall · Hydrus-1D

Introduction

In the unsaturated zone, soil water transport occurs in both the liquid and vapor phases. Using Fick's Law, Penman (1940) investigated liquid and vapor movement in the unsaturated zone. However, Gurr et al. (1952) reported that the results predicted by Fick's Law are higher than the experimentally derived results. Thus, Philip and de Vries (1957) extended the Penman equation to describe the movement of liquid and vapor in the unsaturated zone. In their model, hereafter called the PDV model, the total water fluxes were divided into four components: the thermal liquid, thermal vapor, isothermal liquid and isothermal vapor fluxes. To overcome the phenomena reported by Gurr et al. (1952), they introduced the enhancement factor. Because experimental observation of the enhancement factor is very difficult, Cass (1984) used the pressure head in relation to the heat conductivity to estimate the enhancement factor. Although some workers have questioned the lack of experimental evidence for the existence of the enhancement factor (Webb and Ho 1998) and others have noted that the assumption may not be correct in representative elementary volume (Smits et al. 2011), the PDV model is now commonly used to understand the

---

✉ Jinting Huang
huangjinting79@163.com

[1] Xi'an Institute of Geology and Mineral Resources, No. 438, Youyidong Road, Xi'an 710054, People's Republic of China

[2] Key Laboratory of Subsurface Hydrology and Ecological Effect in Arid Region of Ministry of Education, Chang'An University, No. 126, Yata Road, Xi'an 710054, People's Republic of China

[3] School of Civil Engineering, University College Dublin, Belfield, Dublin 4, Ireland

movement of liquid and vapor in the unsaturated zone after 20 years of discussion (Deb et al. 2011). Current topics of debate involve mathematical solutions (e.g., Saito et al. 2006; Banimahd and Zand-Parsa 2013), the influence of air flow (Zeng et al. 2011), meteorological conditions (Saito and Šimunek 2009), and vegetation cover (Yin et al. 2008; Garcia et al. 2011).

Thermally driven soil water flow is an important process that can affect the water balance and water movement in arid and semi-arid areas (Garcia et al. 2011). Zeng et al. (2009) analyzed the movement of liquid and vapor in the shallow vadose zone and found a diurnal pattern of soil water based on field experimental data taken on sunny days. The effect of solute potential on thermally driven soil water flow has also been considered (Nassar et al. 1989, 1992, 1997). In desert regions, rainfall events can be characterized as rainfall pulses with discontinuous, highly variable, and largely unpredictable frequency and intensity (Schwinning and Sala 2004; Zhao and Liu 2010). Light rainfall only recharges the shallow soil layer, while heavy rainfall can percolate into deep soil layers or groundwater (Li et al. 2013). However, few studies have evaluated the effect of rainfall on coupled fluxes and their temporal variations in desert soil under shallow groundwater level conditions. In particular, information about the movement of liquid water, water vapor, and heat in sandy soil, as well as the pattern of liquid water and water vapor flux, is still limited, as in the Mu Us desert.

In this study, systematic field measurements and simulations using the Hydrus-1D model were conducted to investigate the effect of rainfall on the diurnal pattern of liquid and vapor flux movement in the semi-arid Hailiutu River catchment and parts of the Mu Us desert in northwestern China. The objectives of the study are (1) to describe the diurnal pattern before, during and after a rainfall event and (2) to quantify the predominant forces in those three periods. First, we validated the HYDRUS-1D model (Šimůnek et al. 2012) using soil water and temperature data measured in a field experimental plot. Second, we used the model to investigate the movement of liquid water and water vapor. Third, we analyzed the drivers of liquid water and water vapor movement before, during and after rainfall.

Data and methods

Study site description

The experimental site is located in the Hailiutu River catchment (from 38°06′ to 38°50′N and 108°37′ to 109°15′E) in the Ordos Plateau in northwestern China (Fig. 1). The Hailiutu River is a branch of the Wuding River, which is a major tributary of the Yellow River. The total area of the Hailiutu River catchment is approximately 2645 km^2. A hydrological station located at the outlet of the Hailiutu catchment near Hanjiamao village shows a mean annual discharge of 2.64 m^3/s for the period 1957–2007. Studies show that the flow regime has changed dramatically over the last 51 years. Four major shifts in the flow regime were detected in 1968, 1986, 1992 and 2001, reflecting quasi-natural conditions, reservoir construction, the combination of river diversion and groundwater extraction, and increased crop area, respectively (Yang et al. 2012). Based on the 50 years of meteorological data (from 1957 to 2007) from a station approximately 40 km northwest of the study site, the long-term average annual air temperature is 8.1 °C, and the minimum and maximum monthly average air temperatures are −8.6 °C in January and 23.9 °C in July. The average annual precipitation is 340 mm, approximately 70 % of which occurs between July and September. The average annual potential evaporation is estimated to be 2180 mm (Huang et al. 2015). The area's main crop is maize, which is sown in mid-April and harvested in mid-October, depending on seasonal weather conditions. Irrigation depends on local rainfall.

The experimental site is located approximately 11 km northeast of the Hailutu River. The dominant natural vegetation around the research site is *S. psammophila,* which covers approximately 30 % of the area, along with other sporadically distributed herbs, primarily *Artemisia ordosica*, *Korshinsk peashrub* and *Hedysarum laeve* Maxim. A well was drilled with a Minidiver (DI501, Eijkelkamp, the Netherlands) to monitor changes in the shallow groundwater level. The groundwater table depth (GWT) fluctuated between a maximum of 153.8 cm and a minimum of 89.5 cm, with an average value of 129.9 cm from August 21, 2010 to November 10, 2011. Changes in the GWT can be divided into four periods over a year, which are determined by the groundwater use and climatic conditions. The GWT increased, with fluctuations, from mid-April to mid-October because of vegetation water use and rainfall infiltration. The GWT then decreased from mid-October to mid-November after the cessation of transpiration and groundwater extraction. The GWT fluctuated dramatically from mid-November to the end of March because of the barometric effect during the frozen period. Lastly, the GWT increased from early to mid-April due to thawing soil.

Field measurements

A set of instruments was installed to measure meteorological variables, soil water content, soil temperature and

Fig. 1 Location of the Hailiutu River catchment and the research site

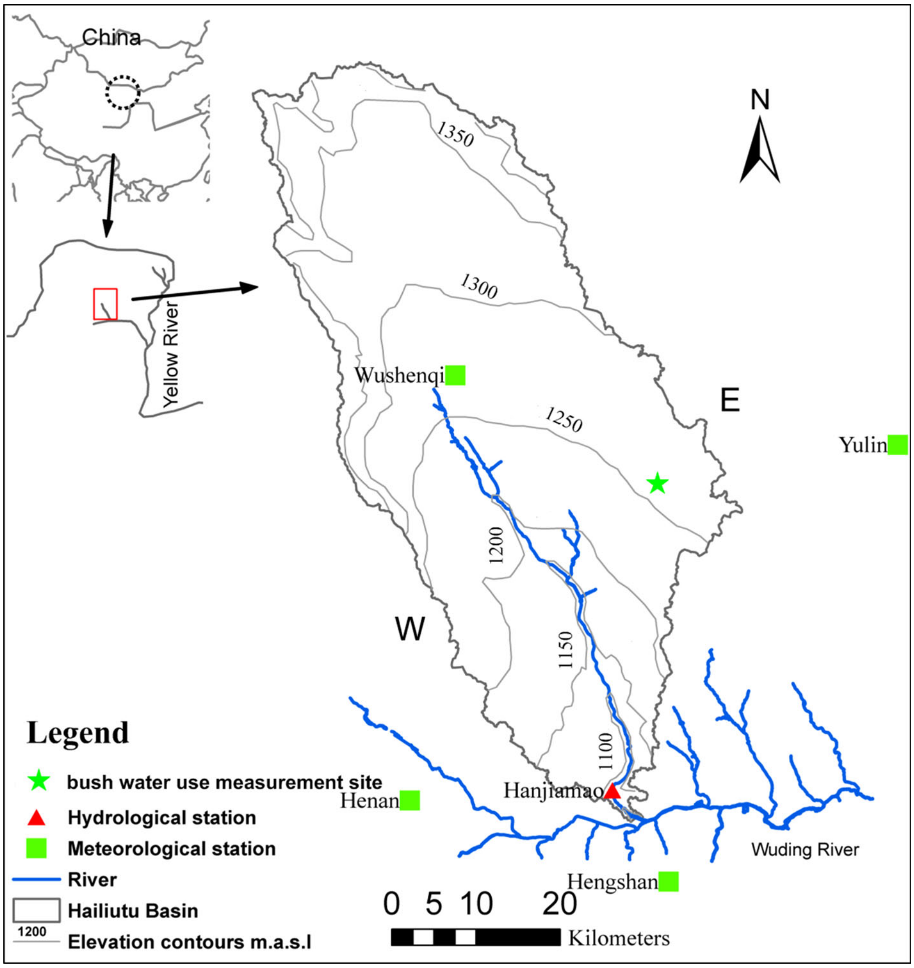

Fig. 2 Photograph of the experimental plot and instrumentation

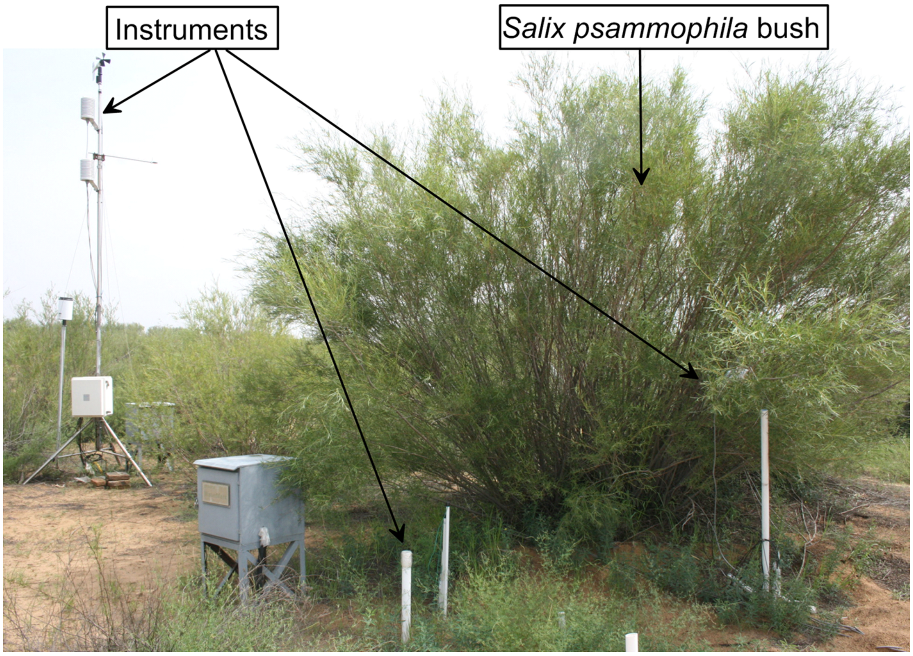

Table 1 Instruments used at the research site

Variable	Height (m)	Horizontal distance to the bush stem (m)	Instrument or sensor type
Wind speed (m/s)	5.25	3.0	05130-5 RM Yong wind monitor
Net radiation (W/m^2)	3.75	3.0	NR-LITE sensor
Rainfall (mm/h)		3.0	52203 RM Young rain gauge
Air temperature (°C) and relative humidity (%)	3.25 4.25	3.0 3.0	HMP45C temperature-humidity sensors
Soil heat flux (W/m^2)	−0.08	3.0	HFP01 heat flow plates
Soil temperature (°C)	−0.02, −0.05,−0.08, −0.2, −0.4, −0.7, −1.0	5.0	TCAV thermocouple
Soil water content (cm^3/cm^3)	−0.05, −0.10	5.0	CS616
	−0.2, −0.4, −0.7 −1.0, −1.2, −1.4	5.0	6005CL2
Groundwater level (cm)	−1.6	1.5	DI501

groundwater level (Fig. 2). The instruments used in the study are listed in Table 1. Detailed information about the river catchment and instruments that were installed at this site can be found in Huang et al. (2015). This study also measured soil water content and soil temperature at the bare soil site.

Measurement of soil water content

At the research site, the unsaturated zone has an approximately 5–15-cm-thick dry layer in the upper soil profile caused by strong evaporation. Thus, two types of sensors with different resolutions were used to measure the soil water contents (SWC, cm^3/cm^3) at eight different depths, both of which used time-domain reflectometry (TDR) technology. All sensors were inserted horizontally into the soil. The sensors installed at depths of 5 and 10 cm were CS616 type (Campbell Scientific, USA, with a resolution of 1 %). Data were recorded at 10-s intervals and stored as 1-h averages using a CR1000 data-logger (Campbell Scientific, USA). The sensors installed at depths of 20, 40, 70, 100, 120 and 140 cm were 6005CL2 type (Wintrase SEC Co. Ltd, USA; 2 % resolution). Data were recorded every 10 s and stored every 4 h with a data logger (Wintrase SEC Co. Ltd, USA).

Measurement of soil temperature

Soil temperature was measured at six different depths using TCAV thermocouple sensors. The measurement depths from the ground surface to the deep soil were 2, 5, 8, 20, 40, 70, 100 cm. All sensors were inserted horizontally into the soil. The data were recorded at 10-s intervals and stored as 1-h averages using a CR1000 data-logger (Campbell Scientific, UAS).

Numerical model for the transport of coupled liquid water, water vapor and heat

Model description

The Hydrus-1D software package (version 4.15, Šimůnek et al. 2012) was used to simulate the coupled liquid water, water vapor and heat transport. The governing equation for one-dimensional vertical flow of liquid water and water vapor in variably saturated media is given by the following mass conservation equation (Saito et al. 2006):

$$\frac{\partial \theta}{\partial t} = -\frac{\partial q_L}{\partial z} - \frac{\partial q_v}{\partial z} \tag{1}$$

where q_L and q_v are the flux densities of liquid water and water vapor (cm/h), respectively; t is time (h); and z is the vertical axis with positive upward (cm).

The flux density of liquid water, q_L, is defined by Philip and de Vries (1957):

$$q_L = q_{Lh} + q_{LT} = -K_{Lh}\left(\frac{\partial h}{\partial z} + 1\right) - K_{LT}\frac{\partial T}{\partial z} \tag{2}$$

where q_{Lh} and q_{LT} are, respectively, the isothermal and thermal liquid water flux densities (cm/h); h is the matric potential head (cm); T is the temperature (°C); and K_{Lh} (cm/h) and K_{LT} (cm^2/°C/h) are the isothermal and thermal hydraulic conductivities for liquid-phase fluxes due to gradients in h and T, respectively.

Using the product rule for differentiation and assuming that relative humidity in soil pores is constant with temperature, the flux density of water vapor, q_v, can be written as follows (Saito et al. 2006):

$$q_v = q_{vh} + q_{vT} = -K_{vh}\frac{\partial h}{\partial z} - K_{vT}\frac{\partial T}{\partial z} \tag{3}$$

where q_{vh} and q_{vT} are the isothermal and thermal water vapor flux densities (cm/h), respectively, and K_{vh} (cm/h) and K_{vT} (cm^2/°C/h) are the isothermal and thermal vapor hydraulic conductivities for water vapor, respectively.

Soil characteristics

The water retention curve (WRC) is one of the fundamental hydraulic functions necessary to solve the soil water flow equation. The soil water retention equation is given by van Genuchten (1980):

$$\theta(h) = \begin{cases} \theta_r + \dfrac{\theta_s - \theta_r}{[1 + |\alpha h|^n]^m} & h \le 0 \\ \theta_s & h > 0 \end{cases} \tag{4}$$

where θ is the volumetric water content (cm^3/cm^3) at pressure head h (cm), θr and θs are the residual and saturated water contents (cm^3/cm^3), respectively, α (>0, in 1/cm) is related to the inverse of the air-entry pressure, and n (>1) is a measure of the pore-size distribution affecting the slope of the retention function ($m = 1-1/n$).

The hydraulic conductivity of soil $K(h)$ is described as follows (van Genuchten1980):

$$K(h) = K_s S_e^l \left\{1 - [1 - S_e^{n/(n-1)}]^{1-1/n}\right\}^2 \tag{5}$$

where K_s is the saturated hydraulic conductivity and S_e is the effective saturation, defined as follows:

$$S_e = \frac{\theta(h) - \theta_r}{\theta_s - \theta_r} \tag{6}$$

To obtain initial values for the hydraulic parameters, in situ saturated hydraulic conductivity was examined using the inverse auger method (Oosterbaan and Nijland 1994). The remaining initial values for soil water retention were estimated by inputting texture data (Table 2) into the Rosetta pedotransfer function model (Schaap et al. 2001) that is included in Hydrus-1D.

The thermal conductivity is defined by de Marsily (1986) as follows:

$$\lambda(\theta) = \lambda_0 + \beta_t C_w |q| \tag{7}$$

where C_w is the volumetric heat capacity of the water, q is the water flux, β_t is the thermal dispersivity (cm), and λ_0 is the baseline thermal conductivity, which was defined the Chung and Horton (1987):

$$\lambda_0 = b_1 + b_2\theta + b_3\theta^{0.5} \tag{8}$$

where b_1, b_2 and b_3 are empirical parameters (W/cm/°C).

Table 2 Soil texture at the research site

Depth (cm)	Sand (%)	Silt (%)	Clay (%)
0–40	97.3	2.7	0
41–55	97.9	2.1	0
56–70	98.5	1.6	0
71–90	98.7	1.3	0
91–110	99.1	0.9	0
111–200	98.8	1.2	0

Boundary and initial conditions

The upper boundary was specified as the 'atmospheric' boundary condition. It is a system-dependent boundary condition in which the soil surface boundary condition may change from a prescribed flux to a prescribed head condition. With sufficient water supply, the evaporation rate is equal to potential evaporation. As the soil dries out, the pressure head reaches a certain value, which is determined by air humidity and air temperature, and then the boundary converts to a pressure head condition. The groundwater level is considered to be the bottom boundary condition according to the field monitor results.

The soil profile was considered to be 200 cm in depth. A spatial discretization of 1 cm was used, leading to 201 nodes across the profile. Calculations were performed for a period of 1523 h from April 28, 2011 at 0:00 to June 30, 2011 at 10:00. Discretization in time varies between a minimum and a maximum time step, controlled by some time step criterion. Except for the aforementioned geometry and time information, it is necessary to specify initial conditions for soil water content in order to use the Hydrus-1D model. The initial soil water content was interpolated at various depths from values measured on April 28, 2011 at 0:00.

Criterion of simulation

The quality of the simulation's results was evaluated with the following relative error (RE) equation:

$$\mathrm{RE} = \frac{|Val_o - Val_s|}{Val_o} \tag{9}$$

where Val_o and Val_s are observed and simulated values, respectively.

Results

Results of measurements

Climatic variables

During the research period (April 28 to June 30, 2011), 89.6 mm of precipitation was measured, including a heavy rainfall event on May 8 that accounted for 59.4 mm. The air temperature varied between 1.7 and 33.0 °C with a daily average of 18.3 °C. The relative humidity varied from 5.8 to 100 % with a daily average of 36.5 %. The net radiation reached a maximum value of 897 W/m^2 at approximately 12:00, and the values were negative during the night. The maximum wind speed was 8.6 m/s, and the daily average was approximately 2 m/s. The net radiation and temperature showed clear diurnal fluctuations, but peaks did not occur at the same time. Relative humidity and wind speed showed more complex variations and changed in opposite directions.

To investigate the effect of rainfall on liquid water and water vapor movement, 4 days were selected to describe changes in climatic variables, May 6–May 9. The climatic variables on May 6 and 7 represented the conditions before rainfall. May 8 and May 9 represented the conditions during and after rainfall, respectively (Fig. 3). Before the heavy rainfall event, the air temperature and net radiation varied diurnally in a quasi-sinusoidal pattern on May 6 and May 7. On those 2 days, maximum and minimum air temperatures were 25.4 and 2.0 °C, respectively. The maximum and minimum net radiation values were 617.4 W/m^2 and −103.1 W/m^2, respectively. Wind speeds were low on May 6 with an average of 1.30 m/s. However, the wind speed increased on May 7 with an average of 3.1 m/s. The air was dry with an average relative humidity of 16.9 % on May 6 and May 7. During and after rainfall, the air temperature and net radiation decreased on May 8 and May 9 to average values of −7.9 W/m^2 and 14.7 °C, respectively. The relative humidity also increased, with an average value of 82.0 % on May 8 and May 9. The wind speed remained low on May 8 and increased on May 9. Interestingly, there was a negative relationship between wind speed and relative humidity, indicating that air moisture was removed by the wind.

Soil temperature

During the experimental period, the soil temperature decreased between the ground surface and the groundwater level. Maximum temperatures were 42.0, 31.8, 24.7, 24.3, 21.3, 18.7, 16.6 and 14.7 °C, corresponding to depths of 2, 5, 8, 20, 40, 70, 100 and 145 cm, respectively. Minimum temperatures were 2.9 °C, 7.8, 10.4, 11.4, 11.7, 10.6, 9.2 and 8.6 °C, corresponding to the same depths as above, respectively. All of the observed soil temperatures increased over the experimental period. Temperatures increased with a quasi-sinusoidal diurnal fluctuation at depths of 2, 5, 8, 20 and 40 cm, with average values of 21.6, 20.3, 18.5, 18.5 and 14.9 °C, respectively. However, the temperature increased steadily, with no diurnal fluctuation, at depths of 70, 100 and 145 cm, with average values of 14.9, 13.1 and 11.7 °C, respectively.

Before the rainfall event, soil temperatures behaved as described above. During and after rainfall on May 8 and May 9, however, soil temperatures decreased steadily in the shallow soil layer (0–40 cm) with no sinusoidal pattern (Fig. 4).

Soil water content at various depths

Soil water content measurements are shown in Fig. 5. During the dry period, the volumetric soil water content (SWC, cm^3/cm^3) decreased with time and was greater with increasing depth. The first rain events on May 8 increased the soil water content both at shallow and deep depths. At a depth of 140 cm, the soil water content remained high throughout the entire period, indicating that the water table is near a depth of 140 cm.

Water table fluctuations

The groundwater table depth (GWT) increased continuously before the heavy rain on May 8 (Fig. 5). The GWT increased in response to the rain events on May 8.

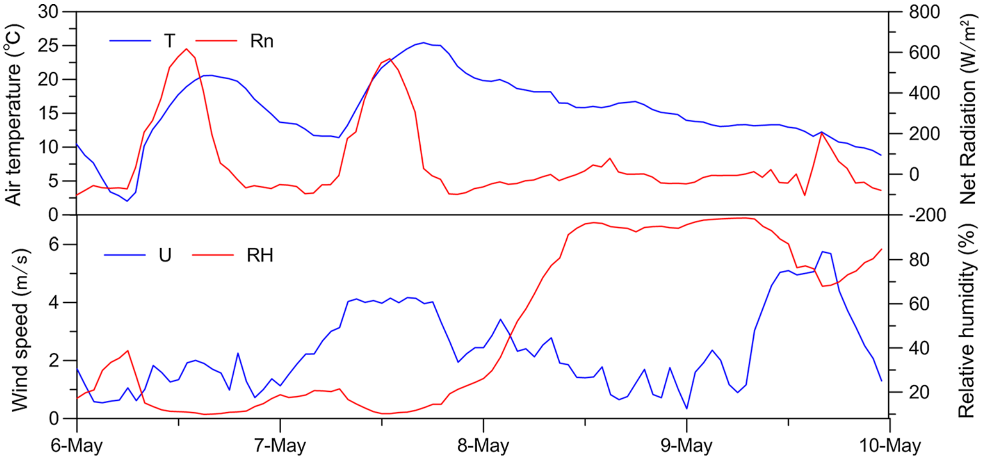

Fig. 3 Measured climatic variables at the research site over the selected period of investigation

Fig. 4 Changes in the soil temperature at different depths over the selected period of investigation

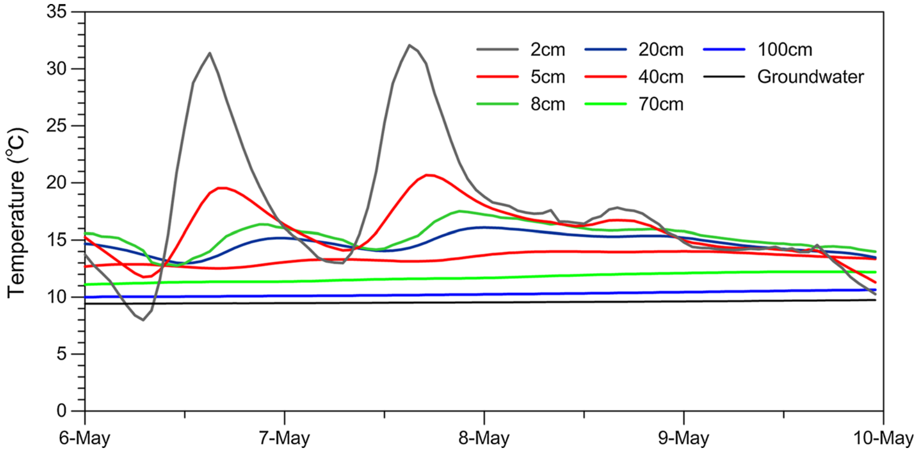

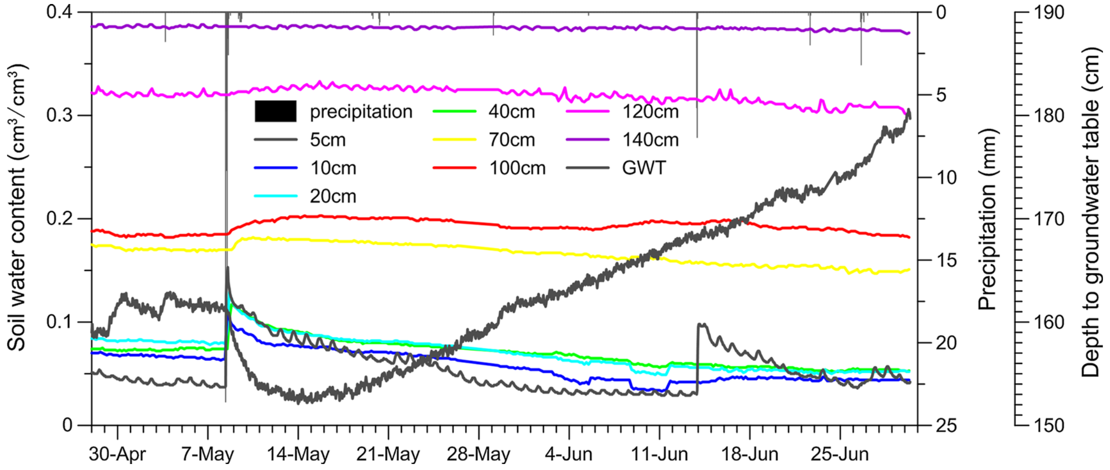

Fig. 5 Soil water content and groundwater table depth at the research site during the period of investigation

Table 3 Relative error of soil water content (SWC) and soil temperature (ST)

Depth (cm)	5	10	20	40	70	100	120	140	145	Total
SWC	0.248	0.139	0.166	0.152	0.023	0.047	0.040	0.046	–	0.108
ST	0.058	0.051	0.018	0.022	0.024	0.022	–	–	0.046	0.035

The temperature at the depth 145 cm refers to the groundwater temperature

Results of model validation

Running the Hydrus-1D model using the Rosetta hydraulic parameter estimates resulted in simulations that were in poor agreement with the field data. Therefore, the soil hydraulic property model was calibrated using the measured soil water contents and soil temperature. In Eqs. (2) and (3), there are six unknown parameters for each layer. When using the inverse model in the Hydrus-1D software, it was found that fitting more than two parameters per layer tended to cause the inverse algorithm to fail. Furthermore, because α and n were more sensitive than the other parameters, all parameters were fixed except for α and n. This method of fitting parameters has also been reported by other researchers (Martinez et al. 2009).

The *RE* of the soil water content at depths of 5, 10, 20, 40, 70, 100, 120, and 140 cm was, respectively, 0.248, 0.139, 0.166, 0.152, 0.023, 0.047, 0.040 and 0.046 (Table 3). The measured water contents were compared with those calculated using the Hydrus-1D model. The predicted and observed soil water contents at all depths are shown in Fig. 6. Generally, the predicted soil water content is similar to the measured data.

Overall, the numerical solution with four layers and α and n fitted for each layer provided the best correlation

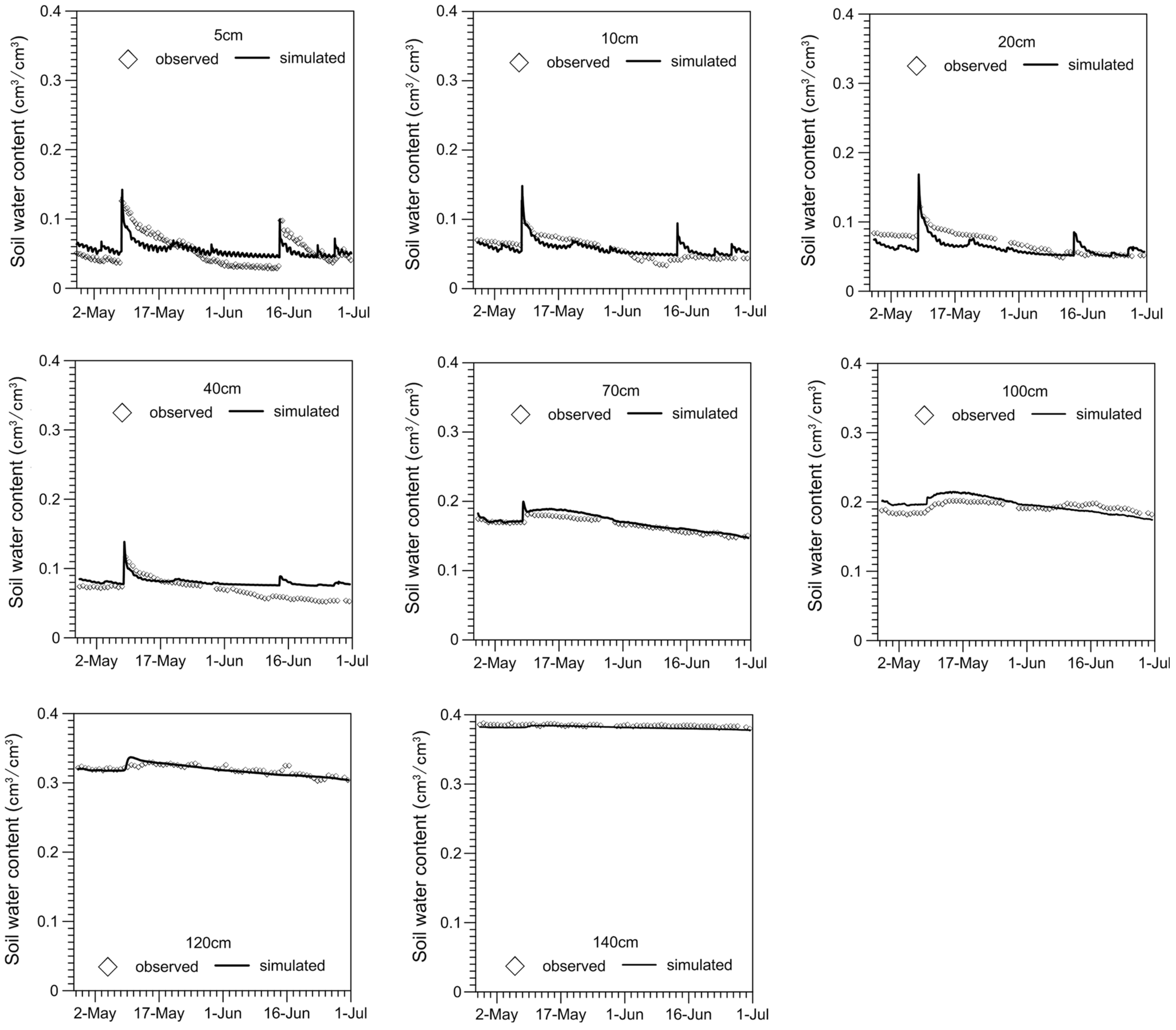

Fig. 6 Fitted results of measured versus simulated soil water content at different depths

Table 4 Fitted hydraulic parameter values

Depth (cm)	θ_r (cm^3/cm^3)	θ_s (cm^3/cm^3)	α (1/cm)	*n* (–)	*K*s (cm/h)	*L* (–)
0–40	0.039	0.39	0.0150	3.980	115.70	0.5
41–55	0.070	0.40	0.0245	3.812	118.22	0.5
56–70	0.070	0.39	0.0198	3.873	113.42	0.5
71–90	0.072	0.39	0.0189	2.916	110.42	0.5
91–110	0.124	0.39	0.0355	2.573	103.02	0.5
111–200	0.065	0.39	0.0162	1.954	110.02	0.5

between measured and simulated water contents, as shown in Table 4.

The *RE* of soil temperature at depths of 5, 8, 20, 40, 70, 100 and 145 cm was 0.058, 0.051, 0.018, 0.022, 0.024, 0.022 and 0.046, respectively (Table 3). The simulated and measured temperatures generally agreed at all seven depths, and the typical sinusoidal diurnal variation of soil temperature was captured (Fig. 7). The fitted heat parameter values are listed in Table 5.

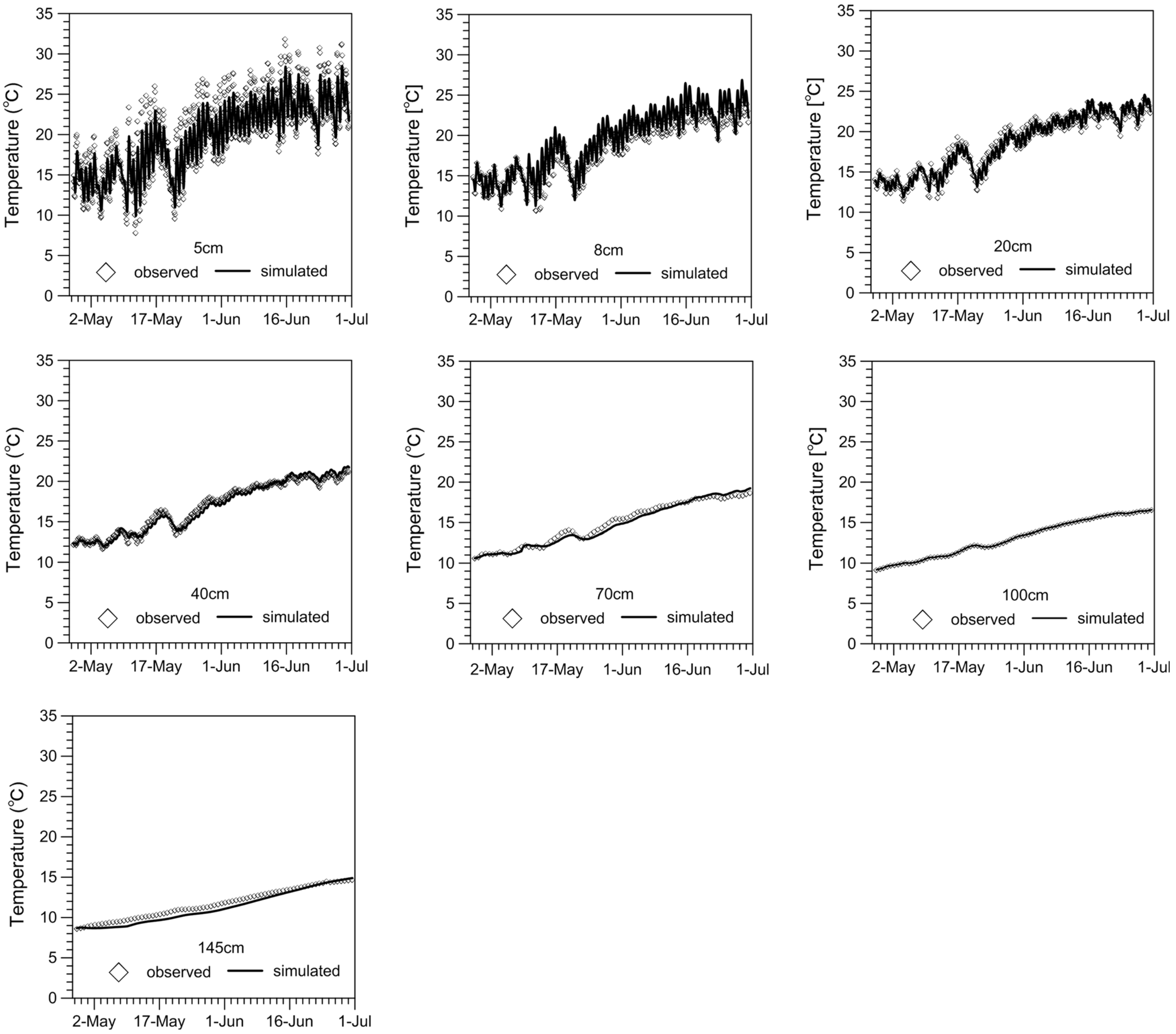

Fig. 7 Measured versus simulated soil temperature at different depths

Table 5 Fitted thermal parameters values

Depth (cm)	Solid	Org.M	Disp	b_1	b_2	b_3	C_n	C_o	C_w
0–40	0.61	0	50.0	128.0	−505.8	1508.9	1496.9	2507.7	4182.1
41–55	0.60	0	50.0	128.0	−505.8	1508.9	1496.9	2507.7	4182.1
56–70	0.61	0	50.0	128.0	−505.8	1508.9	1496.9	2507.7	4182.1
71–90	0.61	0	50.0	128.0	−505.8	1508.9	1496.9	2507.7	4182.1
91–110	0.61	0	50.0	128.0	−505.8	1508.9	1496.9	2507.7	4182.1
111–200	0.61	0	50.0	128.0	−505.8	1508.9	1496.9	2507.7	4182.1

Solid volume fraction of solid phase, *Org.M* volume fraction of organic matter (–), *Disp* longitudinal thermal dispersivity (mm), b_1, b_2, and b_3 are empirical parameters (W/mm/°C), C_n (J/mm^3/°C), C_o (J/mm^3/°C), and C_w (J/mm^3/°C) are volumetric heat capacity of the solid phase, organic matter and the liquid phase, respectively

Movement of liquid water and vapor

During the experimental period, a heavy rainfall event occurred on May 8, so the simulated results of 3 days, May 7–9, were used to analyze the movement of liquid water and vapor affected by rainfall.

The pattern of liquid water and vapor movement

Before the rainfall events

From the change in liquid and vapor fluxes with time forcing by temperature gradient, two stages were identified on May 7. The first stage was characterized by zero fluxes in liquid and vapor, which changed position over time. Based on the direction of the zero flux transition, stage 1 was divided into two periods, the first occurring from 0:00 to 7:00 and the second period from 8:00 to 9:00. During the first period, the zero-flux plane moved upward for both liquid and vapor. At 0:00, the zero-flux plane was found at 3 cm, yet at 7:00, it reached 11 cm (Fig. 8a). During the second period, the zero-flux planes for both liquid and vapor shifted from deep to shallow depths in the soil profile. At 8:00 the zero-flux plane was located at a depth of 11 cm, but at 9:00, the zero-flux plane had reached the ground surface (Fig. 8b).

Figure 8c, d show the liquid and vapor fluxes during stage 2. During this stage, the fluxes moved downward for both liquid water and water vapor. Depending on whether the fluxes were divergent or convergent, stage 2 was also divided into two periods, with the first period from 10:00 to 15:00 and the second period from 16:00 to 0:00. During the first period, both the liquid water and water vapor fluxes were less than zero, which indicates that both liquid and vapor moved downward, though the value approached zero with time. During the second period, the flux direction was the same as during the first period, but it became convergent with time.

Both the flux of liquid water and that of the vapor driven by pressure head had positive values on May 7, except for a difference in effective depth, of 40 and 2 cm, respectively (Fig. 9). The fluxes were also identified as divergent or convergent during the day and night. During the day (7:00 to 19:00), the isothermal liquid flux became non-zero, showing divergent characteristics, but the isothermal vapor flux had convergent characteristics (Fig. 9a). However, these flux characteristics were opposite at night (Fig. 9b).

During the rainfall events

The rainfall event occurred from 9:00 to 14:00 on May 8. Before 9:00, the liquid and vapor fluxes have the same characteristics as during stage 1, on May 7. The changes in the thermal liquid flux and thermal vapor flux are shown in Fig. 10a, which shows that the thermal liquid flux and thermal vapor flux were highly variable from the ground surface to 40 cm in the soil profile. Below 40 cm, both the thermal liquid and thermal vapor fluxes were positive, which indicates a downward flux direction.

Both the isothermal liquid and isothermal vapor fluxes moved downward with almost the same velocity as the infiltration process. At the end of the rainfall event, the position of these fluxes reached 56 cm.

After the rainfall events

After rainfall, the thermal liquid water flux formed more than one zero-flux plane, which indicates a frequent change in direction. In contrast, there was only one zero-flux plane of the thermal vapor flux. Based on the variation in the thermal liquid and thermal vapor flux in the profile after rainfall, two stages can be identified. During the first stage, the thermal liquid flux continued to be variable but its effective depth increased (to 80 cm). However, the thermal vapor flux maintained a negative value, indicating a downward direction (Fig. 11a).

The variation in fluxes during the second stage induced by the temperature gradient is shown in Fig. 11b. A zero-flux plane ranged from the ground surface to 10 cm. The thermal liquid flux was positive, which indicates upward water flow. Below the zero-flux planes (from 10 to 30 cm), the thermal liquid flux had a negative value, indicating downward water flow. Between 30 and 80 cm, the thermal liquid flux remained variable, similar to during rainfall. Between 80 and 110 cm, the thermal liquid water flux had similar characteristics to depths from 10 to 30 cm. There were almost no changes in the thermal liquid flux below a depth of 110 cm. The zero plane of the thermal vapor flux was found in the same position (10 cm) as the thermal liquid flux. This dividing line at the zero-flux plane determined upward and downward thermal liquid flux in the profile. Below a depth of 20 cm, there were no changes over time.

The variations in the isothermal fluxes after rainfall are shown in Fig. 11c. It is apparent that the maximum value of the isothermal liquid flux moved downward over time but maintained a negative value. A cluster of zero-flux planes formed at depths of 30 and 60 to 80 cm. The values of the isothermal vapor flux changed between positive, negative and positive based on these dividing zero-flux planes.

Insight into variations in the liquid water and water vapor fluxes

The model results show that there is a difference in the diurnal pattern of the movement of the liquid water and the

Fig. 8 Movement of liquid water and water vapor driven by the thermal gradient

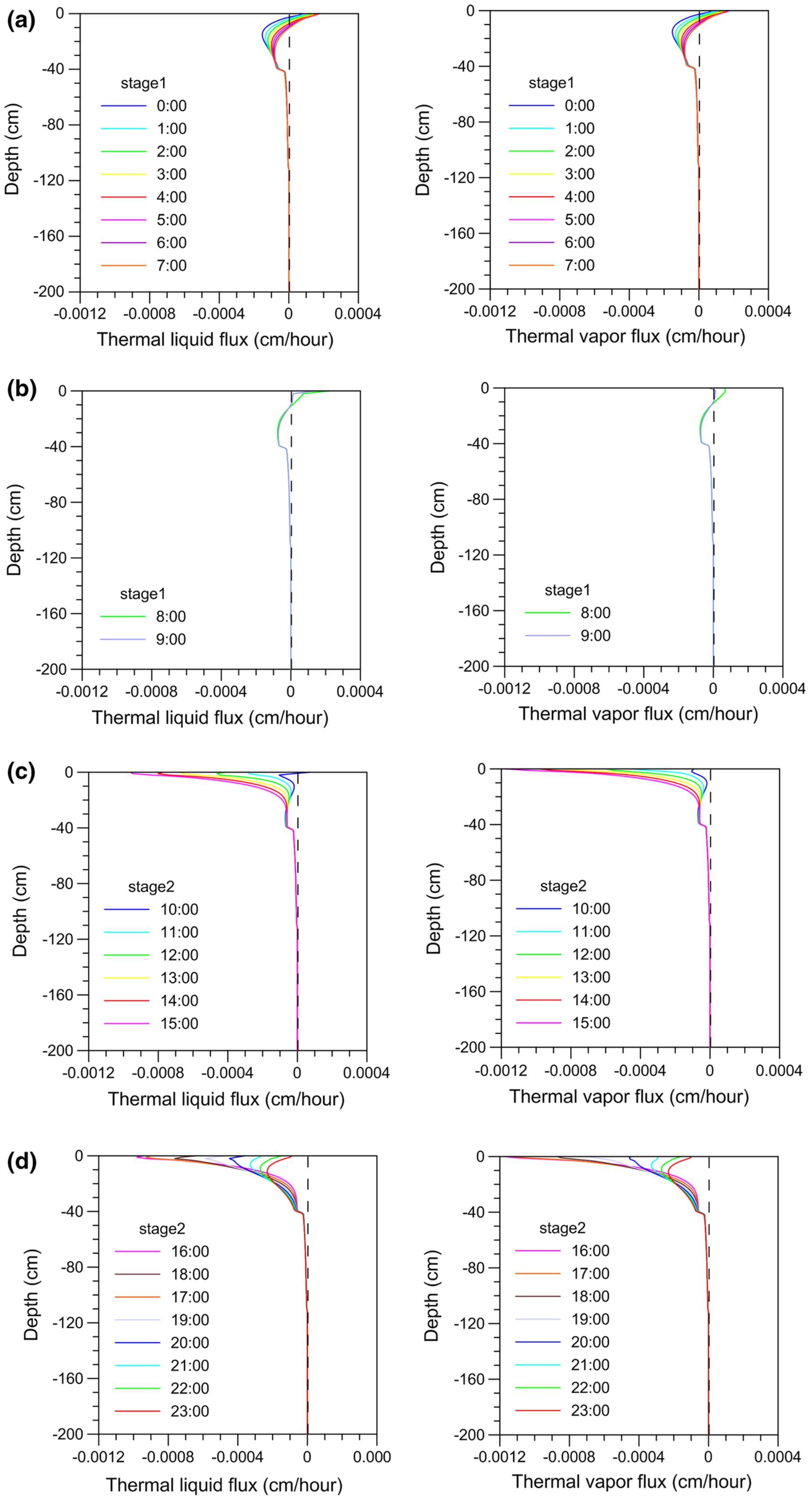

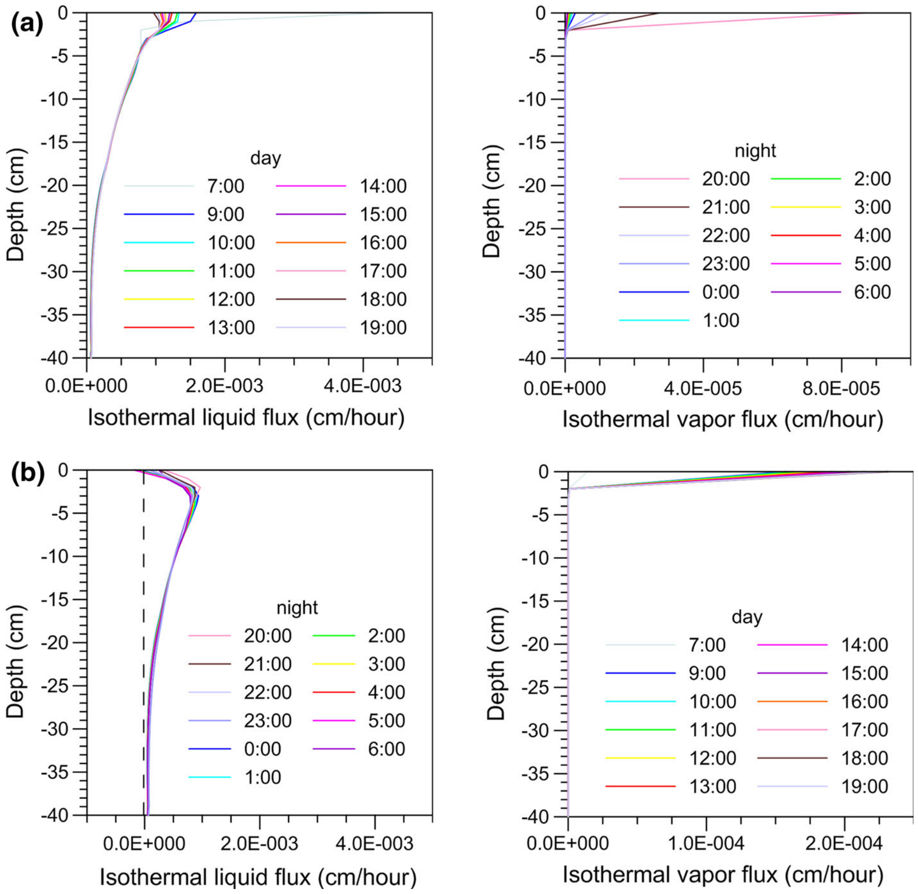

Fig. 9 Divergent (**a**) and convergent (**b**) characteristics of the liquid water and water vapor fluxes driven by the pressure head gradient

water vapor. Differences in the forces driving these changes, as well as hydraulic and heat conductivity, are discussed below.

The driving force

The soil temperature and its changes in gradient throughout the profile are shown in Fig. 12. Figure 12a shows that the temperature decreased from the soil surface to the groundwater table before rainfall. Because of the diurnal fluctuations in air temperature, the soil temperature varied greatly over time. The rainfall event began at 9:00 and ended at 14:00 on May 8. The soil surface temperature decreased from 18.0 °C at 23:00 on May 7 to 13.1 °C at 22:00 on May 8 22:00. After the rainfall, the soil surface temperature gradually increased again due to solar radiation.

The isoline density indicates how strongly the soil temperature at a certain depth fluctuated. Dense and sparse isolines represent the rapid and slow variations in soil temperature with time, respectively. Figure 12b shows that the isolines from 0 to 70 cm were denser than those from 70 to 200 cm, which indicates rapid changes in soil temperature in the shallow profile. Furthermore, approximately May 7 10:00, the soil temperature gradient transitioned from positive to negative at the soil surface. The soil surface temperature gradient remained negative until May 8 19:00. From 20:00 to 22:00 on May 8, the temperature gradient became positive.

Figure 13 shows the pressure head and its changes in gradient during the selected period. Before the rainfall event, the values of pressure head increased between the ground surface and the bottom of the soil profile. During the rainfall event, the balance of pressure head was disrupted and infiltration began. Figure 13b shows that the greatest density of pressure head gradient isolines occurred in the very shallow soil profile (at approximately 5 cm) before and after rainfall. During rainfall and the infiltration process, the greatest density of pressure head gradient isolines moved downward and finally the value of the gradient became 1, which indicates that the rain had infiltrated the groundwater.

The hydraulic and thermal conductivity

The movement of liquid and vapor is controlled not only by temperature and pressure head gradient but also by the hydraulic and thermal conductivity. The functions for the

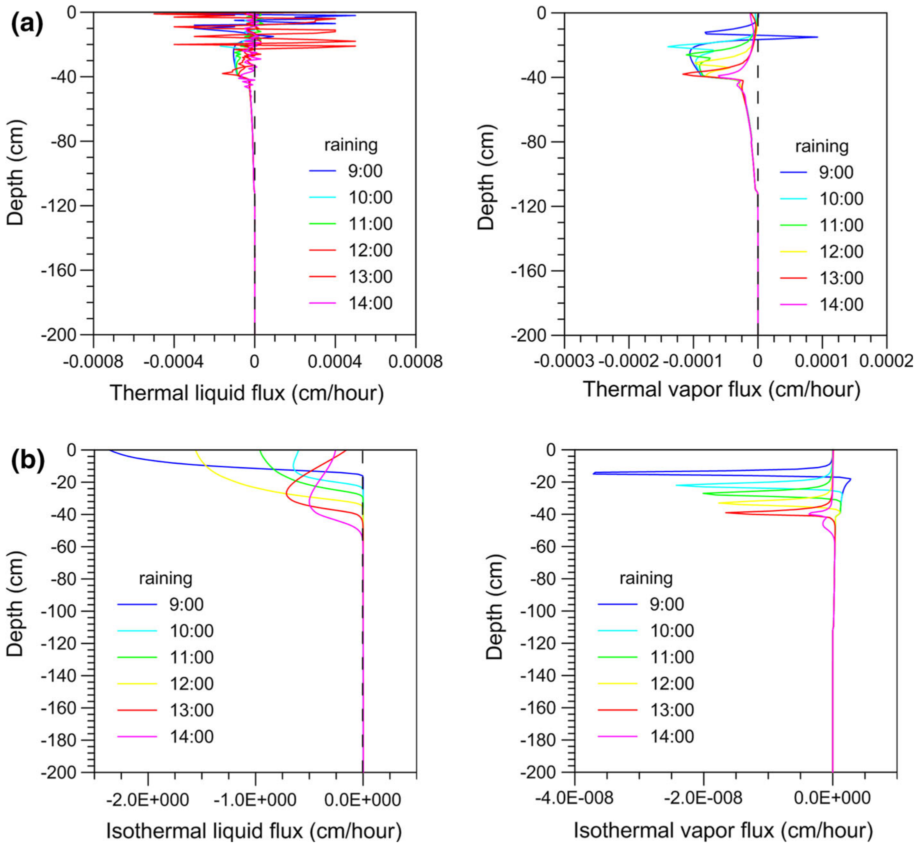

Fig. 10 Variation in thermal and isothermal liquid and vapor flux during rainfall

thermal hydraulic conductivities are defined as follows (Noborio et al. 1996; Fayer 2000):

$$K_{\mathrm{LT}} = K_{\mathrm{Lh}}\left(hG_{\mathrm{wT}}\frac{1}{\gamma_0}\frac{d\gamma}{dT}\right) \tag{8}$$

$$K_{\mathrm{vh}} = \frac{D_{\mathrm{v}}}{\rho_{\mathrm{w}}}\rho_{\mathrm{vs}}\frac{\mathrm{Mg}}{\mathrm{RT}}H_{\mathrm{r}} \tag{9}$$

$$K_{\mathrm{vT}} = \frac{D}{\rho_{\mathrm{w}}}\eta H_{\mathrm{r}}\frac{d\rho_{\mathrm{sv}}}{dT} \tag{10}$$

where K_{Lh} is the isothermal unsaturated hydraulic conductivity (cm/h), which is decided by van Genuchten's (1980) model; G_{wT} is the gain factor (dimensionless), which assesses the temperature dependence of the soil water retention curve and is set as 7 for sand (Noborio et al. 1996); γ is the surface tension of soil water (J/cm^2); D is the water vapor diffusivity in soil (cm^2/h); ρ_{vs} is the saturated vapor density (kg/cm^3); η is the enhancement factor (dimensionless); ρ_{w} is the density of liquid water (g/cm^3); *Hr* is the relative humidity (dimensionless) and is expressed as *EXP*(*hMg/RT*); *M* is the molecular weight of water (g/mol); *g* is the gravitational acceleration (cm/s^2); and *R* is the universal gas constant (mol/K).

Comparison between the changes in liquid water and vapor in space and time over the experimental period demonstrates that the penetration depth of the liquid water and water vapor mainly fluctuated above 100 cm in the profile. Therefore, variations in the isothermal liquid hydraulic conductivity, thermal liquid hydraulic conductivity, isothermal vapor hydraulic conductivity and thermal vapor hydraulic conductivity above 100 cm are shown in Fig. 14a–d, respectively.

Figure 14a shows that the values of K_{Lh} are all positive, ranging from 0 to 0.85 cm/h. From May 7 at 0:00 to May 8 at 9:00, K_{Lh} values were smaller than 0.05 cm/h throughout the profile. Due to the effect of rainfall, K_{Lh} values fluctuated from large to small to large again between 10:00 and 15:00 on May 8. Furthermore, dense isolines between 0 and 40 cm indicate that strong variations in K_{Lh} occurred over that interval. After the rainfall event, these values decreased as the water flow moved downward. Values of K_{LT} were slightly smaller than K_{Lh}, ranging from −0.02 to 0.32 cm/K/h (Fig. 14b). The pattern of K_{LT} was similar to that of K_{Lh} before, during and after the rainfall event except at shallow depths (0–10 cm).

The values of K_{vh} and the K_{vT} were smaller than those of K_{Lh} and K_{LT} by at least three orders of magnitude (Fig. 11c, d). Values of K_{vh} and K_{vT} ranged from 0 to 2.4E-9 and from 0 to 2.0 E-3, respectively. Before the rainfall event, the values of K_{vh} and K_{vT} decreased from the ground

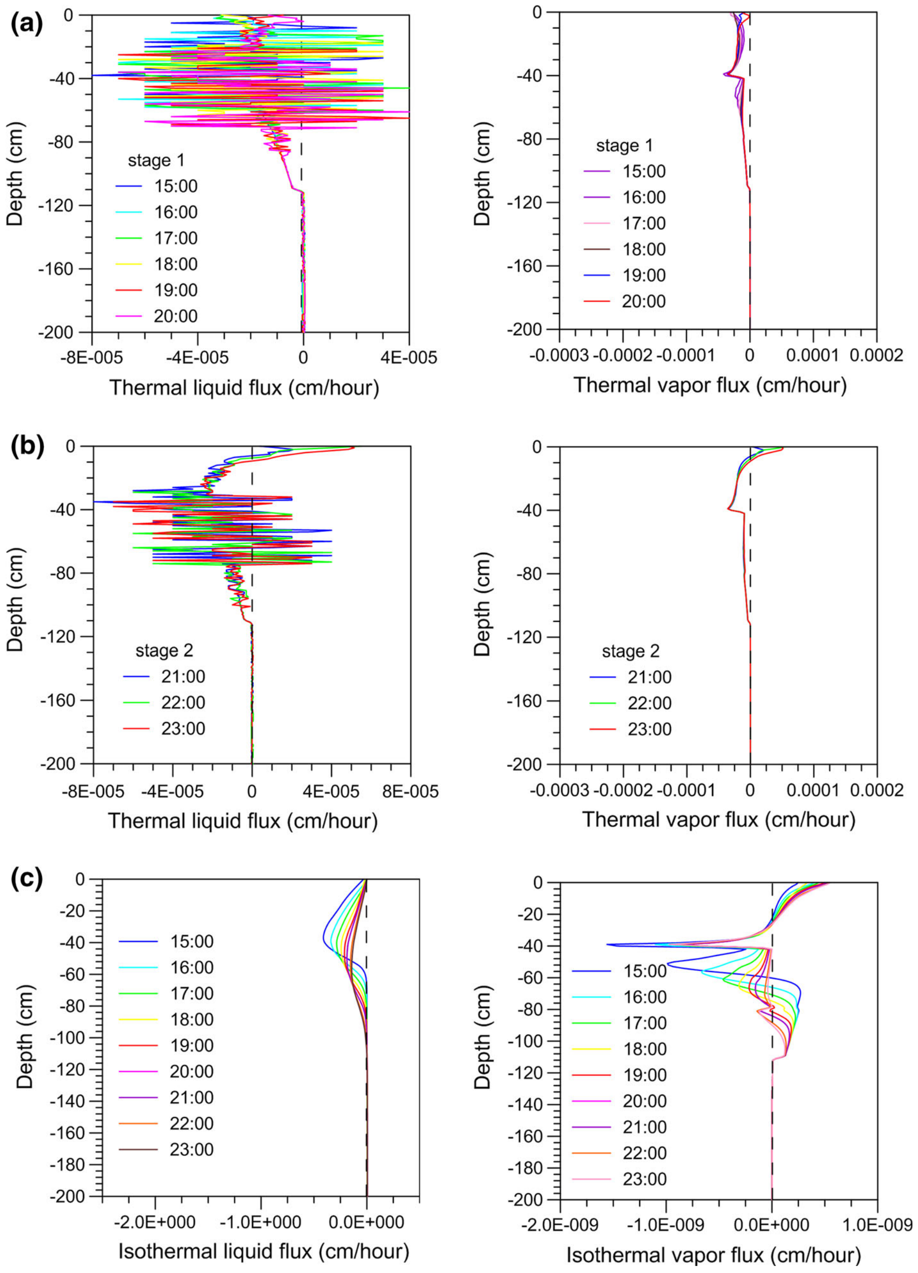

Fig. 11 Variation in thermal and isothermal liquid and vapor flux after rainfall

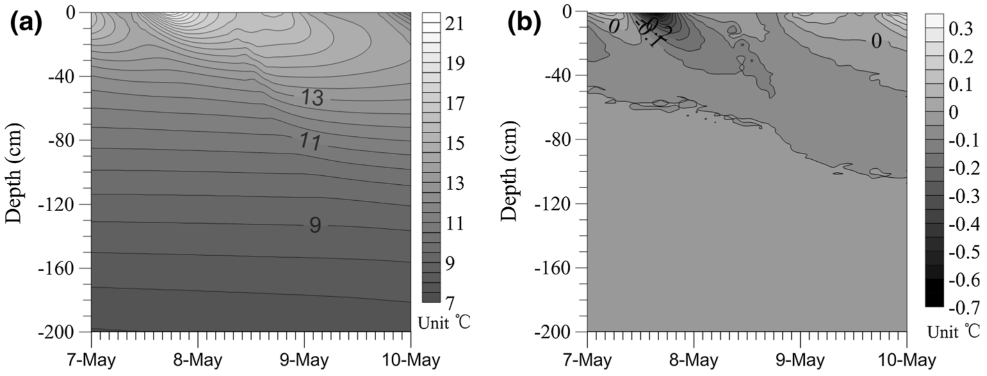

Fig. 12 Time series of soil temperature in the profile from May 7 to May 9 (**a**) and its gradient (**b**)

Fig. 13 Time series of pressure head in the profile from May 7 to May 9 (**a**) and its gradient (**b**)

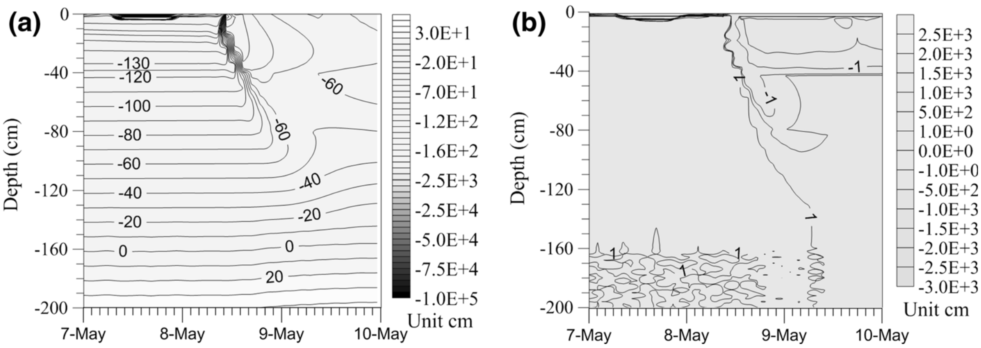

Fig. 14 Time series of conductivity in the profile from May 7 to May 9, with **a** isothermal liquid hydraulic conductivity; **b** thermal liquid hydraulic conductivity; **c** isothermal vapor hydraulic conductivity; and **d** thermal vapor hydraulic conductivity

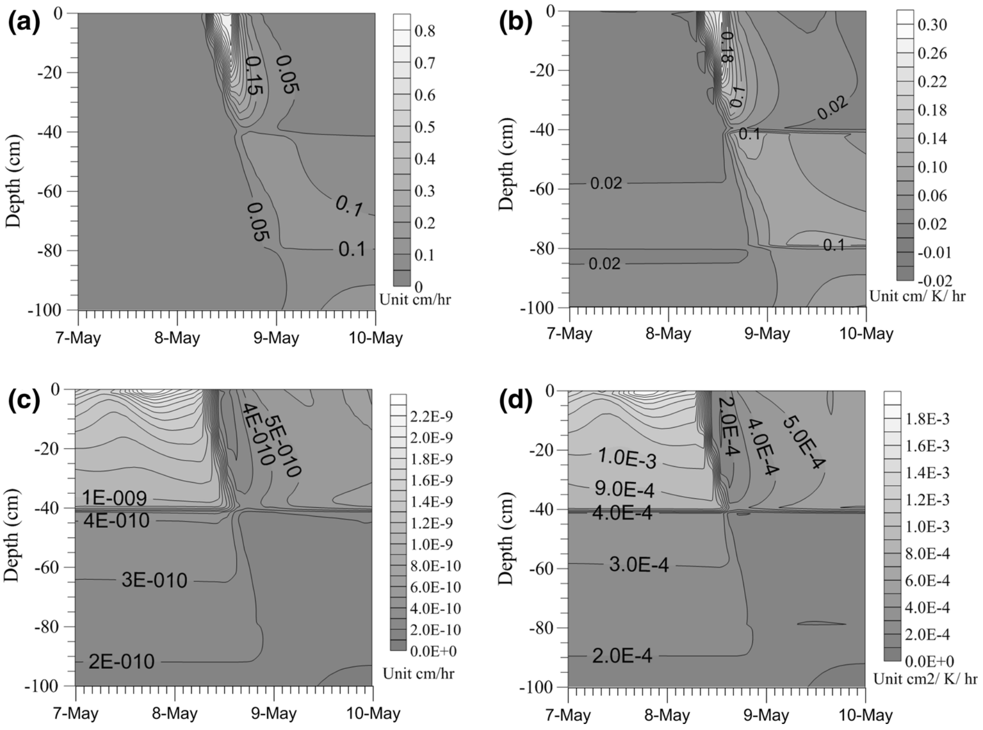

surface down through the profile. During the rainfall event, isolines were very dense, and the values decreased further. Until the end of the experimental period, K_{vh} and K_{vT} did not return to the same values as before the rainfall event, though they exhibited large trends. Therefore, Fig. 14 shows that the rainfall event increased the liquid hydraulic conductivity but decreased the vapor conductivity.

Conclusions

The diurnal pattern of liquid water and water vapor movement is strongly affected by rainfall events, as shown by analysis of variations in fluxes, driving forces and hydraulic conductivities. Based on the results presented, we draw the following conclusions.

On May 7, when no rainfall occurred, both the thermal vapor and thermal liquid fluxes had zero planes during the first stage (from 0:00 to 9:00) with convergence at the ground surface. These zero planes disappeared during the second stage (from 10:00 to 23:00). The vapor and liquid fluxes driven by the pressure head gradient showed different characteristics during day versus night in the shallow soil layer. The isothermal liquid fluxes were divergent at the ground surface during the day but convergent during the night. Interestingly, the isothermal vapor fluxes showed opposite characteristics as the liquid fluxes; that is, they were convergent during the day but divergent during the night. This phenomenon indicates that the divergence and convergence of liquid water and water vapor driven by pressure head mainly occurs in the shallow soil layer during sunny days.

During the rainfall event, the balance between liquid water and water vapor movement was disrupted. Because of large changes in the hydraulic gradient and hydraulic conductivity, the thermal liquid and vapor fluxes were highly variable with small values. In contrast, the isothermal liquid and vapor fluxes moved downward gradually and steadily.

After the rainfall event, the percolation process continued; so, the thermal liquid and vapor fluxes retained the same characteristics as during rainfall. However, the zone of high variability moved downward. Above that zone, the thermal liquid and vapor fluxes resumed the pattern they had exhibited before rainfall. The percolation planes of the isothermal liquid fluxes continued downward and converged on the ground surface. The isothermal vapor fluxes formed zero planes at different depths in the profile.

Acknowledgments This study was supported by the National Natural Science Foundation of China (41102160; 41472220), the Ministry of Land and Resources of the People's Republic of China (201311076), the Fundamental Research Funds for the Central Universities (2013G1502030) and the Natural Science Foundation of Shaanxi Province (2014JQ5187; 2015KJXX-69). The authors are grateful to the reviewers; the comments and suggestions of the reviewers have contributed significantly to the improvement of the manuscript.

References

Banimahd SA, Zand-Parsa S (2013) Simulation of evaporation, coupled liquid water, water vapor and heat transport through the soil medium. Agr Water Manage 130:168–177

Cass A, Campbell GS, Jones TL (1984) Enhancement of thermal water vapor diffusion in soil. Soil Sci Soc Am J 48:25–32

Chung SO, Horton R (1987) Soil heat and water flow with a partial surface mulch. Water Resour Res 23:2175–2186

de Marsily G (1986) Quantitative hydrogeology. Academic Press, London

Deb SK, Shukla MK, Sharma P, Mexal JD (2011) Coupled liquid water, water vapor, and heat transport simulations in an unsaturated zone of a sandy loam field. Soil Sci 176:387–398

Fayer MJ (2000) UNSAT-H Version 3.0: unsaturated soil water and heat flow model-theofy, user manual and examples, Pacific Northwest National Laboratory, Washingto, p 331

Garcia CA, Andraski BJ, Stonestrom DA, Cooper CA, Simunek J, Wheatcraft SW (2011) Interacting vegetative and thermal contributions to water movement in desert soil. Vadose Zone J 10:552–564

Gurr CG, Marshall TJ, Hutton JT (1952) Movement of water in soil due to a temperature gradient. Soil Sci 74:335–345

Huang JT, Zhou YX, Yin LH, Wenninger J, Zhang J, Hou GC, Zhang EY, Uhlenbrook S (2015) Climatic controls on sap flow dynamics and used water sources of *Salix psammophila* in a semi-arid environment in northwest China. Environ Earth Sci 73:289–301

Li X, Zhang Z, Huang L, Wang X (2013) Review of the ecohydrological processes and feedback mechanisms controlling sand-binding vegetation systems in sandy desert regions of china. Chinese Sci Bull 58:1483–1496

Martinez JJ, Skaggs TH, van Genuchten MT, Candela L (2009) A root zone modeling approach to estimating groundwater recharge from irrigated areas. J Hydrol 367:138–149

Nassar IN, Horton R (1989) Water transport in unsaturated non-isothermal salty soil: II. Theoretical development. Soil Sci Soc Am J 53:1330–1337

Nassar IN, Horton R (1992) Simultaneous transfer of heat, water, and solute in porous media: I. Theoretical development. Soil Sci Soc Am J 56:1350–1356

Nassar IN, Horton R (1997) Heat, water, and solution transfer in unsaturated porous media: I—theory development and transport coefficient evaluation. Transp Porous Med 27:17–38

Noborio K, McInnes KJ, Heilman JL (1996) Two-dimensional model for water, heat, and solute transport in furrow-irrigated soil: I. Field evaluation. Soil Sci Soc Am J 60(4):1010–1021

Oosterbaan RJ, Nijland HJ (1994) Determing the saturated hydraulic conductivity. In H.P. Titzema, ed. Drainage principles and applications, pp 435–475. 2nd edition. ILRI Publication 16. Wageningen, The Netherlands, ILRI

Penman HL (1940) Gas and vapor movements in soil: the diffusion of vapors through porous solids. J Agr Sci 30:437–462

Philip JR, de Vries DA (1957) Moisture movement in porous materials under temperature gradients. Trans Am Geophys Union 38:222–232

Saito H, Šimůnek J (2009) Effect of meteorological models on the solutions of the surface energy balance and soil temperature variations in bare soils. J Hydrol 373:545–561

Saito H, simunek J, Mohanty BP (2006) Numerical analysis of coupled water, vapor, and heat transport in the vadose zone. Vadose Zone J 5(2):784–800

Schaap MG, Leij FJ, van Genuchten MTh (2001) Rosetta: a computer program for estimating soil hydraulic parameters with hierarchical pedotransfer functions. J Hydrol 251:163–176

Schwinning S, Sala OE (2004) Hierarchy of responses to resource pulses in arid and semi-arid ecosystems. Oecol 141:211–220

Šimůnek J, Šejna M, Saito H, Sakai M, van Genuchten M Th (2012) The Hydrus-1D software package for simulating the one-dimensional movement of water, heat, and multiple solutes in variably-saturated media. Version 4.15. Department of environmental sciences university of California riverside riverside, California

Smits KM, Cihan A, Sakaki T, Illangasekare TH (2011) Evaporation from soils under thermal boundary conditions: experimental and modeling investigation to compare equilibrium- and nonequilibrium-based approaches. Water Resour Res 47(5):143–158

van Genuchten MTh (1980) A closed-form equation for predicting the hydraulic conductivity of unsaturated soils. Soil Sci Soc Am J 44:892–898

Webb SW, Ho CK (1998) Review of enhanced vapor diffusion in porous media, SAND-98-1819C; CONF-980559

Yang Z, Zhou YX, Wenninger J, Uhlenbrook S (2012) The causes of flow regime shifts in the semi-arid Hailiutu River, Northwest China. Hydrol Earth Syst Sc16:87–103

Yin J, Young MH, Yu Z (2008) Effects of paleoclimate and time-varying canopy structures on paleowater fluxes. J Geophys Res 113:304–312

Zeng YJ, Wan L, Su ZB, Saito H, Huang KL, Wang XS (2009) Diurnal soil water dynamics in the shallow vadose zone (field site of China University of Geosciences, China). Environ Geol 58:11–23

Zeng YZ, Su ZB, Wan L, Wen J (2011) A simulation analysis of the advective effect on evaporation using a two-phase heat and mass flow model. Water Resour Res 47(10):582

Zhao W, Liu B (2010) The response of sap flow in shrubs to rainfall pulses in the desert region of china. Agr Forest Meteorol 150:1297–1306